Schweizerische Eidgenossenschaft
Confédération suisse
Confederazione Svizzera
Confederaziun svizra

Federal Department of the Environment, Transport, Energy and Communications DETEC

Swiss Federal Office of Energy SFOE
Energy Research and Cleantech

Final report dated 27.11.2020

BIOPEC

Photoelectrochemical glycerol reforming towards production of renewable hydrogen and chemicals

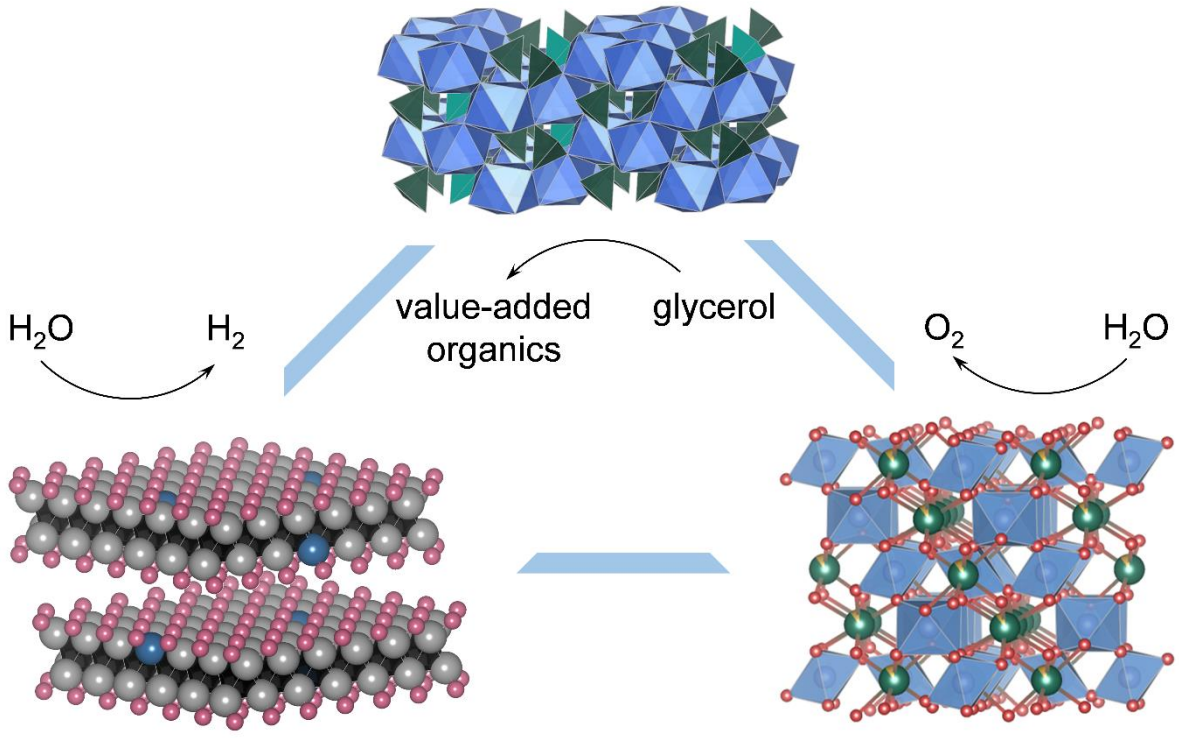

Source: ©Denis Kuznetsov 2020

Date: 27.11.2020

Location: Bern

Publisher:
Swiss Federal Office of Energy SFOE
Energy Research and Cleantech
CH-3003 Bern
www.bfe.admin.ch

Authors:
Christoph Müller, ETH Zürich, muelchri@ethz.ch
Denis Kuznetsov, ETH Zürich, denisk@ethz.ch

SFOE project coordinators:
Stefan Oberholzer, stefan.oberholzer@bfe.admin.ch

SFOE contract number: SI/501598-01

Summary

1. A photoanode based on a $BiVO_4$ semiconductor coupled with atomic layer deposited nickel oxide was exploited for the photoelectrocatalytic water and glycerol decomposition. The performance of the assembled architecture rivals that of state-of-the-art materials, e.g. TiO_2.

2. A family of $Y_{1.8}M_{0.2}Ru_2O_{7-\delta}$ pyrochlore oxides was investigated as model catalysts for the oxygen evolution reaction (OER) in order to reveal the physical origin of the metal substitution effect on the catalytic activity. The fundamental understanding obtained enabled us to propose new general guidelines towards the design of materials with enhanced OER performance.

3. A member of the novel family of two-dimensional materials, single metal site-substituted Mo_2CT_x (T_x = O, OH, F) MXene, was explored as an electrocatalyst for the hydrogen evolution reaction (HER). Excellent activity and stability in HER make Mo_2CT_x:Co a promising candidate to replace platinum for the large scale hydrogen production from water.

Contents

1 Introduction

1.1 Background information and current situation

Molecular hydrogen H_2 is a promising energy carrier, which can be used directly in emission free fuel cell devices,[1-2] or in hydrogenation reactions to produce high-energy-density chemicals such as ammonia[3] or methanol.[4] Conventionally, hydrogen is produced by the reforming of fossil fuels thus contributing appreciably to industrial CO_2 emissions.[5] Electrolysis of water[6] offers a potentially sustainable alternative way for H_2 synthesis, if coupled with renewable electricity sources such as wind, hydropower or sunlight-driven photovoltaics.[7-8] Complementing water splitting, the (photo)electrochemical (PEC) oxidation of cheap and abundant organics or biomass feedstocks (*e.g.* glycerol) is an emerging field with enormous potential for the production of hydrogen and value added chemicals.[9-10] While the splitting of water into H_2 and O_2 is highly endothermic (ΔG^o = 237 kJ mol^{-1}), requiring a minimum cell voltage of ΔE^o = 1.23 V, supplemented by the reaction overpotential (typically > 0.5 V to achieve industrially relevant current densities), the dehydrogenative reforming of abundant carbohydrates or alcohols requires a relatively low external energy input. Moreover, the products of the partial oxidation of organic feedstocks can be of high market value. Yet the highly efficient catalysts composed of abundant elements for the reforming of organic species are not developed, in part as a result of a limited fundamental understanding of the reaction pathways of the organics valorisation to selectively produce H_2 and valuable oxygenates. In this regard, formulating the new fundamental design principles leading to the synthesis of novel catalysts would be highly beneficial for the area.

The use of semiconductor electrodes in a photoelectrochemical setup allows to reduce considerably the reaction overpotentials, paving the way towards unbiased solar-driven photocatalysis.[11] In the present study, we evaluate the performance of $BiVO_4$-based photoanodes for the photoelectrocatalytic reforming of glycerol, $C_3H_5(OH)_3$. Glycerol, a side product of biodiesel production, is a highly abundant and inexpensive chemical formed during the transesterification of triglycerides with methanol (one mole of glycerol is generated per three moles of biodiesel,[12] which corresponds to *ca.* 100 kg of glycerol produced per ton of biodiesel). Oxidation, or the partial dehydrogenative reforming of glycerol, can in principle generate a plethora of the high value-added chemicals, *e.g.* 1,3-dihydroxyacetone, glyceraldehyde, tartronic acid, glycolic acid or hydroxypyruvic acid (Scheme 1). On the other hand, the complete dehydrogenative decomposition of one mole of glycerol can generate up to four moles of hydrogen at a relatively low energy input (ΔG = 3.9 kJ $mol_{glycerol}^{-1}$).[13] Therefore, glycerol has a potential to be used in both H_2 generating electrolyzers and direct alcohol fuel cells.[14-15]

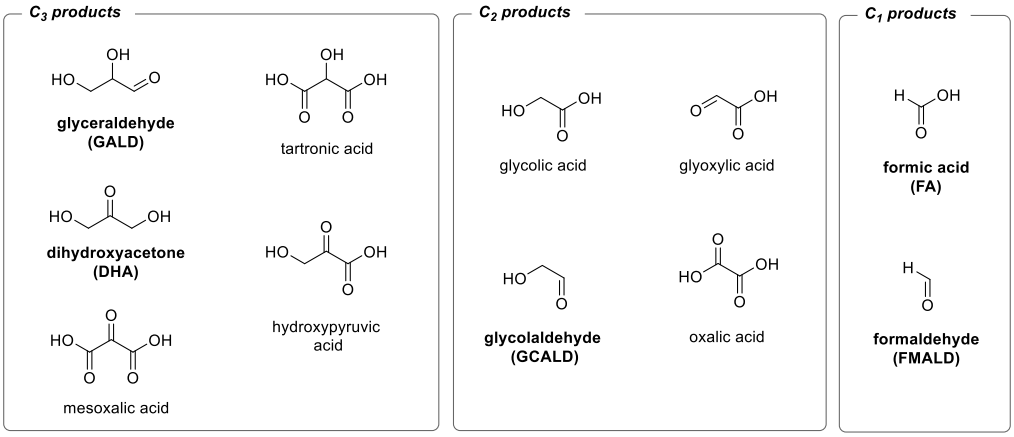

Scheme 1. Products of electrochemical glycerol reforming identified in the literature. Products found in this study are shown in bold.

1.2 Purpose of the project

The efficiency of the photoelectrochemical production of fuels from water/organics decomposition reactions relies primarily on the properties of the three essential components: (1) semiconducting material, which serve as photoanode/photocathode, enabling the conversion of the energy of irradiation into a chemical potential; (2) (co-)catalyst, which can be coupled with a photoabsorber, for the anodic half-reaction (water/organics oxidation half-reaction, which is the major source of the energy losses); in case of organics (glycerol) decomposition, the co-catalyst also strongly affects the reaction selectivity; (3) (co-)catalyst for the cathodic hydrogen evolution reaction (HER). Thus, the research program targeted to provide insights into the design of efficient materials for the applications outlined above.

1.3 Objectives

1.3.1. Bismuth vanadate selected in this study has been identified as one of the most promising photoanodes, exploited initially for water splitting.[16] In its monoclinic phase, $BiVO_4$ is a photoactive n-type semiconductor with a bandgap of 2.4 eV,[17-18] *i.e.* it absorbs in the visible light range. However, unmodified $BiVO_4$ features low catalytic activity in photoelectrochemical water oxidation. To enhance kinetics, improve charge transport characteristics and reduce surface recombination of the photo-generated charge carriers in $BiVO_4$, different strategies have been employed, *i.e.* aliovalent doping or deposition of co-catalysts for the oxygen evolution reaction.[19] Despite these advances, $BiVO_4$ remained so far underutilized for the reforming of abundant organic feedstock molecules to H_2 and partially-oxidized value-added organic chemicals.

1.3.2. Highly active OER catalysts demonstrate excellent performance in catalysis for further oxidation reactions, particularly in glycerol oxidation. Towards this goal, we targeted to establish a rational design principles of complex oxide catalysts for oxygen evolution, which can be used for the design of novel compositions for OER and, hence, glycerol oxidation. As a model system, we have selected the $A_2Ru_2O_{7-\delta}$ pyrochlore family due to its high activity in oxygen evolution and the structural flexibility of pyrochlores enabling the incorporation of various substituents both on the A and B site.

1.3.3. Platinum is the state-of-the-art catalyst for the hydrogen evolution reaction, however low abundance and high cost of Pt preclude its widespread implementation motivating for the search of new catalytically active materials comprised of earth-abundant elements. In this regard, early transition metal carbides can be seen as promising candidates for the use in commercial electrolyzers.[20]

2 Procedures and methodology

The synthesis of the materials was performed using published ($BiVO_4$, $A_2Ru_2O_{7-\delta}$) or original techniques developed in this study (Mo_2CT_x:M, ALD-deposited NiO_x on $BiVO_4$). Characterization of the composition and morphology of the materials was performed using powder X-ray diffraction (XRD), scanning electron microscopy (SEM) and transmission electron microscopy (TEM). X-ray photoelectron spectroscopy (XPS), X-ray absorption spectroscopy (XAS) and DFT calculations were employed to reveal the electronic features of the materials. (Photo)electrochemical measurements were performed using standard electrochemical techniques using commercial or custom-made two- or three-compartment electrochemical cells with or without illumination. Product analysis for glycerol oxidation reaction was performed using high performance liquid chromatography (HPLC) and ^1H and ^{13}C NMR techniques. Degradation of the electrode materials was followed by inductive coupled plasma (ICP) analysis.

3 Results and discussion

3.1. Engineering $BiVO_4$-based photoanodes for solar-driven valorisation of glycerol

To improve water/glycerol oxidation kinetics and mitigate anodic photocorrosion of $BiVO_4$, we have applied atomic layer deposition (ALD), which enabled us to produce a uniform overcoating of $BiVO_4$ with metal oxide of a desired composition. Such an overlayer can serve as a protection coating preventing $BiVO_4$ from dissolution and as a co-catalyst for anodic water/glycerol oxidation. Nickel oxide was selected as the material of choice due to its high activity for water oxidation in different environments.[21] Electrodes containing W-doped $BiVO_4$ films on fluorine doped tin oxide (FTO) coated glass substrates were fabricated by a slightly modified electrodeposition-calcination method.[22-23] The tungsten dopant was introduced into $BiVO_4$ during the calcination step in order to enhance the bulk charge transfer efficiency of the material[24] (denoted W:$BiVO_4$). Nickel oxide was coated onto W:$BiVO_4$-based electrodes via atomic layer deposition (ALD)[25] using pulses of nickelocene ($Ni(\eta^5\text{-}C_5H_5)_2$, $NiCp_2$) and H_2O at 250 °C. The as-deposited NiO_x/W:$BiVO_4$ electrodes (Ni content of 0.65 at%) were used for PEC measurements without further thermal treatment.

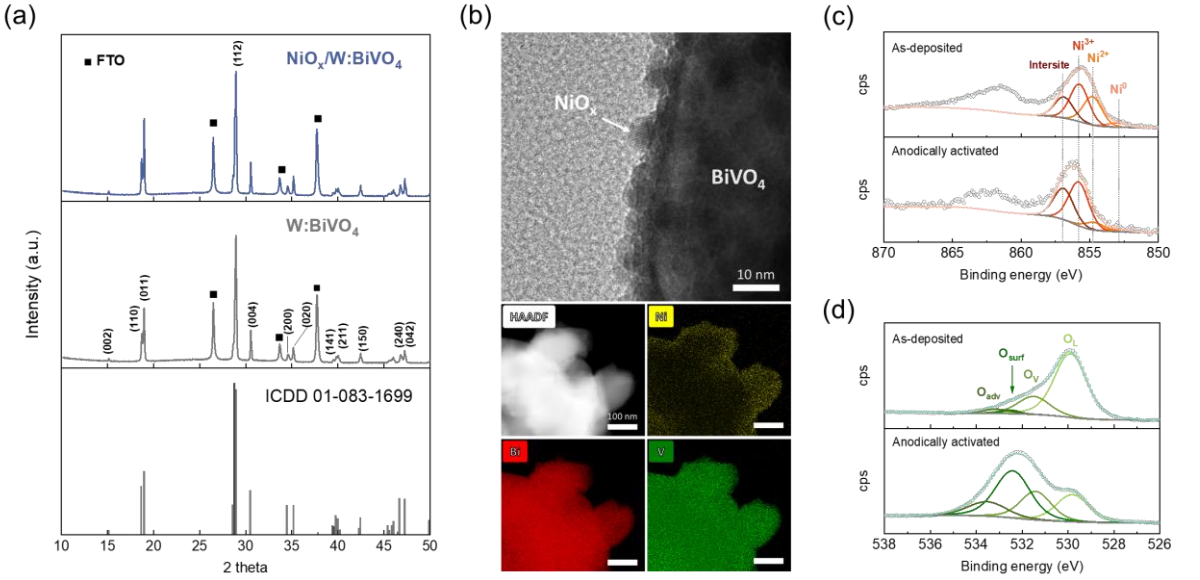

Figure 1. (a) XRD patterns of $BiVO_4$ (ICDD No. 01-083-1699), W:$BiVO_4$ and as deposited NiO_x/W:$BiVO_4$. The peaks corresponding to the FTO substrate are indicated by squares. (b) HRTEM, HAADF-STEM, and EDX elemental mapping images of electrochemically activated NiO_x/W:$BiVO_4$ electrodes. Overlay of the (c) Ni 2p and (d) O 1s core level XPS signals of as-deposited and electrochemically activated NiO_x/W:$BiVO_4$.

X-ray diffraction (XRD) pattern of the as-synthesized W:$BiVO_4$ matches that of a monoclinic scheelite reference (No. 01-083-1699, ICDD database, Fig. 1a). No additional peaks were observed in the diffraction pattern of NiO_x/W:$BiVO_4$, *i.e.* after atomic-layer-deposition of NiO_x onto W:$BiVO_4$ (Fig. 1a). The NiO_x/W:$BiVO_4$ electrodes were subjected to five anodic scans, from −0.05 to 1.50 V_{RHE} in 0.5 M potassium borate buffer solution (KB_i, pH = 9.3), and then used for glycerol oxidation. Such electrochemical activation yields $NiO_y(OH)_z$ species (denoted NiO_x) in the form of uniformly distributed crystallite nanoparticles on the surface of W:$BiVO_4$, according to high-resolution transmission electron microscopy (HRTEM), high-angle annular dark-field scanning transmission electron microscopy (HAADF-STEM) and energy dispersive X-ray spectroscopy (EDX) elemental mapping (Fig. 1b). XRD of the anodically-activated NiO_x/W:$BiVO_4$ electrodes is identical to that of the as prepared NiO_x/W:$BiVO_4$.

The surface composition and valence states of as-deposited and anodically activated NiO_x were probed by X-ray photoelectron spectroscopy (XPS). The Ni 2p core level XPS spectrum of as-deposited NiO_x reveals features ascribed to metallic Ni, Ni^{2+} and Ni^{3+} at 852.9, 854.7 and 855.7 eV, respectively, while an additional feature at a higher binding energy (denoted as intersite, 856.9 eV) can be ascribed to the presence of defects in the nickel (oxy)hydroxide structure (Figure 1c).[26] As expected, anodic activation increased the relative amount of oxidized nickel species ($NiO_x(OH)_y$), evidenced by the much enhanced intensity of the feature at 855.7 eV. The O 1s core level spectrum (Figure 1d) of the as-deposited and activated NiO_x/W:$BiVO_4$ films can be deconvoluted into four components: lattice oxygen (O_L, 529.5 eV), lattice oxygen sites located in the vicinity of oxygen vacancies/defects (O_V, 531 eV), surface oxygen species (O_{surf}, 532 eV), and adventitious species (weakly bound adsorbed water/CO_2, O_{adv}).[27] Comparison of the spectra of the as-deposited and activated films reveals a distinct increase in the concentration of surface oxygen groups for the electrochemically activated films, *i.e.* an increase from 2 to 42 %, consistent with the formation of layered $Ni(OH)_2$/$NiO_y(OH)_z$ species with a highly exposed surface.[28]

To investigate the performance of NiO_x/W:$BiVO_4$ electrodes in photoelectrochemical glycerol oxidation, PEC studies were carried out using a custom-made, two-compartment cell with an anion-exchange membrane. As glycerol decomposition can generate a plethora of the high market value chemicals (e.g. 1,3-dihydroxyacetone, glyceraldehyde, tartronic acid, glycolic acid, hydroxypyruvic acid), we have studied glycerol oxidation reaction (GOR) on W:$BiVO_4$-based photoanodes under varying electrolyte environments, in the presence/absence of the co-catalyst to investigated their influence on the reaction selectivity and identify conditions favouring the formation of certain products. Thus, glycerol oxidation was studied in mild alkaline media (0.5 M potassium borate buffer, KB_i, pH = 9.3) and in a non-buffered electrolyte (0.5 M Na_2SO_4, pH = 7.0), which gradually acidifies during the PEC reaction.

Fig. 2a shows linear sweep voltammetry (LSV) profiles under dark and illumination conditions for W:$BiVO_4$ and NiO_x/W:$BiVO_4$ in 0.5 M KB_i and 0.5 M Na_2SO_4 electrolytes. In Na_2SO_4 solution, the PEC performance of W:$BiVO_4$ is characterized by an onset potential of *ca.* 0.43 V_{RHE} and a photocurrent for water oxidation of 2.3 mA cm^{-2} at 1.2 V_{RHE} (in the absence of glycerol). The NiO_x co-catalyst enhances the photocurrent to 3.3 mA cm^{-2} (1.2 V_{RHE}), leading to a *ca.* 50 mV cathodic shift of the onset potential. In the presence of glycerol (0.1 M), the photocurrent increases in the entire potential range, reaching 4.2 mA cm^{-2} at 1.2 V_{RHE}.

In mild-alkaline conditions (0.5 M KB_i), W:$BiVO_4$ and NiO_x/W:$BiVO_4$ exhibit *ca.* 50 mV cathodic shift of the onset potential on the RHE scale relative to that in the Na_2SO_4 electrolyte (Fig. 2b). The photocurrent for NiO_x/W:$BiVO_4$ electrodes reaches 2.5 mA cm^{-2} (0.8 V_{RHE}) and increases to 3.5 mA cm^{-2} at 1.2 V_{RHE}, thus matching or exceeding the performance of some transition-metal-oxide-based PEC systems (*e.g.* TiO_2) employed for the oxidation of organic alcohols (methanol, ethanol or glycerol).[29] Control experiments show a high reproducibility of the data collected on W:$BiVO_4$ and NiO_x/W:$BiVO_4$ photoelectrodes. Overall, the enhancement of the catalytic activity of NiO_x/W:$BiVO_4$ for water and glycerol oxidation in mildly alkaline conditions relative to neutral conditions may originate from the pH-dependence of the electrocatalytic activity of the NiO_x co-catalyst layer, which is a typically observed phenomenon for nickel or cobalt-based (oxy)hydroxides.[30]

The charge-transfer dynamics at the semiconductor-electrolyte interface were analysed by the transient photocurrent profile at a constant potential. The initial transient photocurrent, I_{in}, is caused by the separation of the photogenerated hole-electron pairs, where trapping or recombination of charge carriers takes place by surface states or reduced species in an electrolyte.[31] The continuous decay of the photocurrent indicates ongoing recombination until a steady state, I_{st}, is reached. Here, we used alkaline 0.5 M KB_i conditions and relatively low biases, *i.e.* 0.3 V_{RHE}, 0.5 V_{RHE}, and 0.8 V_{RHE} (Fig. 2c). In the absence of glycerol, the steady-state photocurrent at 0.3 V_{RHE} (*i.e.* close to the onset potential) is nearly zero for W:$BiVO_4$ and NiO_x/W:$BiVO_4$ electrodes, coinciding with the onset potential observed in the LSV profile. In the presence of glycerol, a distinct non-zero photocurrent is detected reaching 0.08 mA cm^{-2} (0.3 V_{RHE}), 0.53 mA cm^{-2} (0.5 V_{RHE}) and 1.22 mA cm^{-2} (0.8 V_{RHE}) for the W:$BiVO_4$ electrodes (Fig. 2c). In addition, the back-reaction current was significantly suppressed at 0.3 V_{RHE}, likely

indicating a reduced accumulation of holes at the material surface. In the presence of glycerol, the photocurrent of the $NiO_x/W:BiVO_4$ electrodes increased to 0.2 mA cm^{-2} (0.3 V_{RHE}), 1.2 mA cm^{-2} (0.5 V_{RHE}) and 2.9 mA cm^{-2} (0.8 V_{RHE}). Together with an increased transient decay time (Fig. 2d), these observations are evidence for faster kinetics of the photoelectrochemical glycerol oxidation reaction as compared to the oxygen evolution reaction (OER) in water.

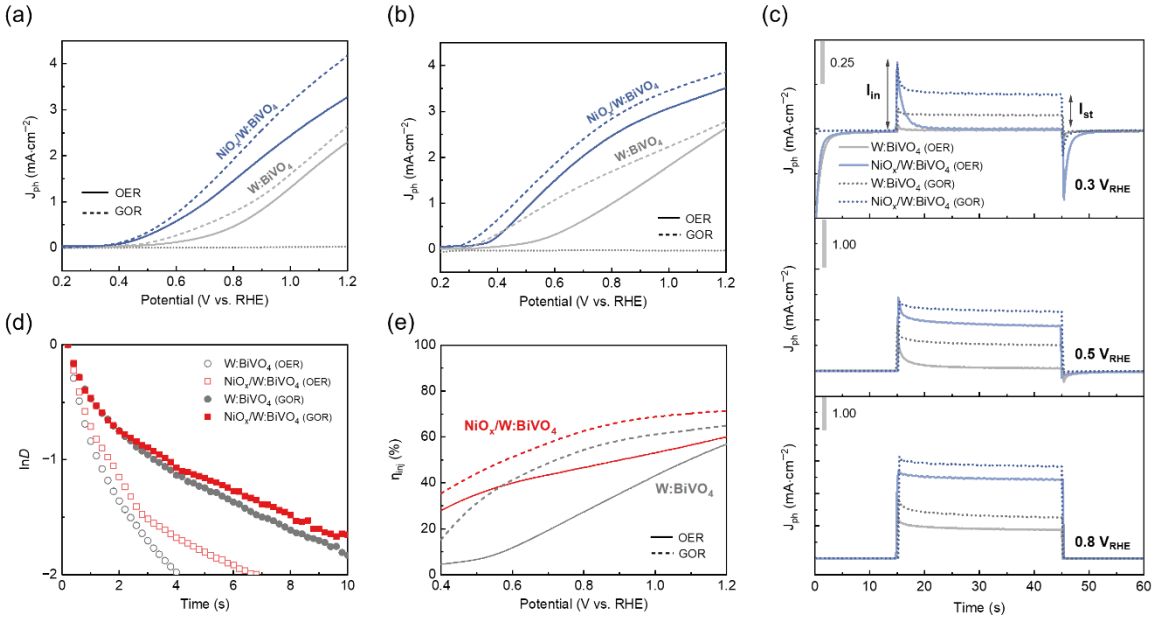

Figure 2. Linear sweep voltammetry of $W:BiVO_4$ and $NiO_x/W:BiVO_4$ in (a) 0.5 M Na_2SO_4 and (b) 0.5 M KB_i with and without the addition of 0.1 M glycerol under dark and AM 1.5, 100 mW cm^{-2} illumination. (c) Chopped chronoamperometry plots of $W:BiVO_4$ and $NiO_x/W:BiVO_4$ in 0.5 M KB_i with (dotted lines) and without (solid lines) 0.1 M glycerol at 0.3 V_{RHE}, 0.5 V_{RHE}, and 0.8 V_{RHE}. The color code is the same as on panels a-b. (d) Plots of ln*D* as a function of time of photoanodes for water oxidation and glycerol oxidation (E = 0.5 V_{RHE}). (e) Hole injection efficiency vs. applied bias for glycerol oxidation in 0.5 M KB_i.

Finally, the hole injection efficiency for water oxidation, estimated using sulfite anion (SO_3^{2-}) as a hole scavenger was measured, reaching *ca.* 55% and 65% on $W:BiVO_4$ and $NiO_x/W:BiVO_4$ electrodes, respectively, at 1.2 V_{RHE} (Fig. 2e). In the presence of glycerol (0.1 M), the $NiO_x/W:BiVO_4$ photoelectrode exhibits a superior hole transfer to glycerol than $W:BiVO_4$ throughout the whole potential window, reaching an efficiency of 72% at 1.2 V_{RHE}, that additionally confirms the enhancement of the kinetics of glycerol oxidation with respect to OER.

Next, the C_1-C_3 products of glycerol oxidation during long-term glycerol electrolysis (10 h) over $W:BiVO_4$ and $NiO_x/W:BiVO_4$ electrodes were identified and quantified by ^1H and ^{13}C NMR spectroscopy and high performance liquid chromatography (HPLC). The effect of the NiO_x catalyst layer and the applied bias on the production rate (R) and faradaic efficiency (FE) of the detected products of the glycerol oxidation is illustrated in Fig. 3, based on ^1H NMR spectra and chromatography results. The distribution of the products of the electrolysis reaction depends on the applied potential, type of the electrolyte and the electrode material (Table 1). Specifically, in the 0.5 M Na_2SO_4, the average production rate of DHA, GALD, GCALD and FA increases with increasing potential when using the $W:BiVO_4$ electrode (Fig. 3a). At 0.8 V_{RHE}, FA is a primary product of glycerol oxidation on the $W:BiVO_4$ electrodes with a FE of over 70 % and a production rate of *ca.* 54 mmole h^{-1} m^{-2}, while at the higher potential of 1.2 V_{RHE}, a four-fold and five-fold enhancement of the production rate of DHA (70 mmol h^{-1} m^{-2}) and GCALD (*ca.* 60 mmol h^{-1} m^{-2}), corresponding to FE's of 19 % and 11 %, is observed.

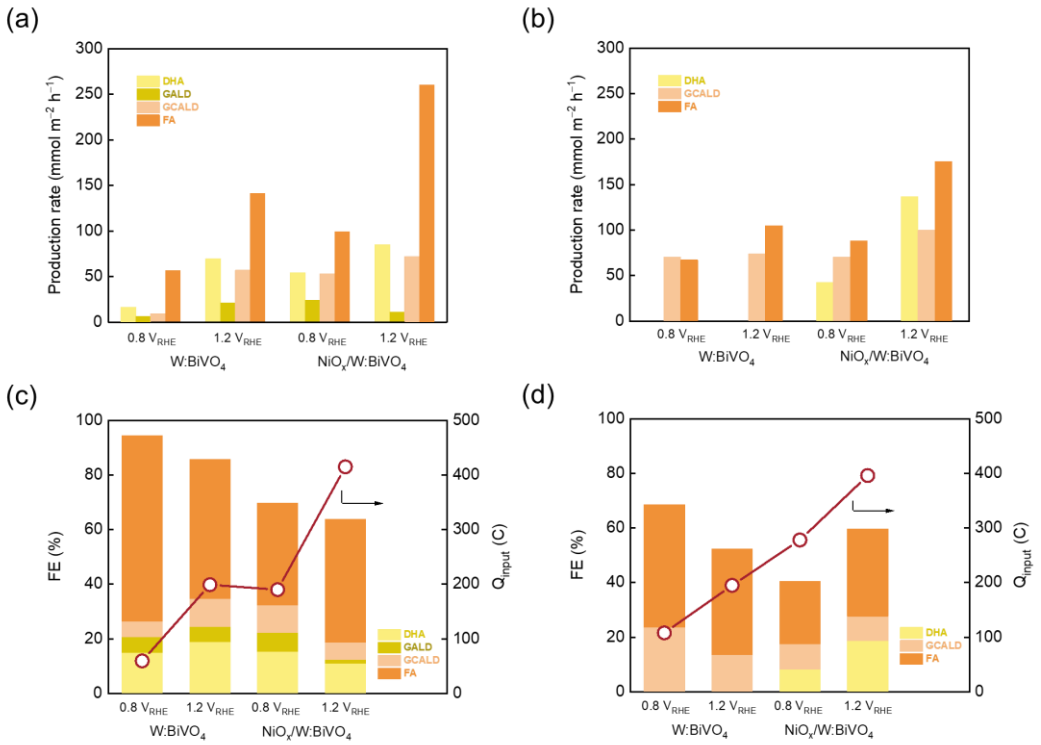

Figure 3. Quantitative product analysis for different electrolytes after 10 h of continuous photoelectrolysis of 0.1 M glycerol solution over W:$BiVO_4$ and NiO_x/W:$BiVO_4$ electrodes at different applied voltages. Production rate (R, mmol m^{-2} h^{-1}) determined in (a) 0.5 M Na_2SO_4 and (b) 0.5 M KB_i; Faradaic efficiency per mole of specific compound (FE, %; bars) and total charge transfer (Q_{input}, C; line) determined in (c) 0.5 M $Na_2SO_{4(aq)}$ and (d) 0.5 M KB_i using HPLC and ^{1}H NMR.

For both 0.5 M Na_2SO_4 and 0.5 M KB_i electrolytes, the deposition of a NiO_x catalyst layer results in an enhanced catalytic glycerol oxidation reflected in the higher photocurrents (higher total charge transfer) and product yields. For instance, at an electrolysis potential of 1.2 V_{RHE} in 0.5 M Na_2SO_4, a *ca.* two-fold increase of the photocurrent was achieved upon deposition of a NiO_x co-catalyst. In addition, an increase in the applied bias increases the production rate of the value-added DHA in the presence of NiO_x. Specifically, in 0.5 M KB_i, a three-fold enhancement of production rate of DHA (138 mmol h^{-1} m^{-2}) was achieved at 1.2 V_{RHE} (compared to 0.8 V_{RHE}) along with an improved FE of 19 % (Figure 3b and Figure 3d).

In 0.5 M Na_2SO_4, PEC glycerol oxidation using a W:$BiVO_4$ electrode leads to higher amounts of GALD and GCALD at increased applied bias (1.2 V_{RHE} vs. 0.8 V_{RHE}). In contrast, NiO_x/W:$BiVO_4$ electrodes preferentially produce GALD and GCALD at a lower potential, 0.8 V_{RHE}, presumably due to their overoxidation at higher applied voltages. Although the deposition of a NiO_x co-catalyst does not appear to alter the general reaction pathway, the presence of a nickel catalyst strongly influences the product distribution (which is also affected by the applied bias and reaction media). For instance, NiO_x/W:$BiVO_4$ electrodes show an increased selectivity toward DHA formation over GCALD at 1.2 V_{RHE} in an alkaline KB_i buffer. In contrast to a recent report, in which it was argued that the selective formation of DHA from glycerol is feasible,[32] our findings indicate that multiple products inevitably form upon glycerol photoelectrooxidation, emphasizing in turn the importance of the use of complementary analytical tools (*e.g.* HPLC and NMR spectroscopy) for an accurate quantitative analysis of the complex product mixture.

Table 1. Composition of products from 10 h photoelectrochemical glycerol oxidation.

Electrolyte	Electrode	Applied bias	Identified products	Enhanced rate or FE of specific products observed with increased potential
Na_2SO_4	W:$BiVO_4$	0.8 V_{RHE}	GALD, DHA, GCALD, FA, FMALD	R_{DHA}, R_{GALD}, R_{GCALD}, R_{FA} FE_{DHA}, FE_{GALD}, FE_{GCALD}
		1.2 V_{RHE}	GALD, DHA, GCALD, FA, FMALD	
	NiO_x/W:$BiVO_4$	0.8 V_{RHE}	GALD, DHA, GCALD, FA, FMALD	R_{DHA}, R_{GCALD}, R_{FA}
		1.2 V_{RHE}	GALD, DHA, GCALD, FA, FMALD	
KB_i	W:$BiVO_4$	0.8 V_{RHE}	GALD, GCALD, FA, FMALD	R_{FA}
		1.2 V_{RHE}	GALD, GCALD, FA, FMALD	
	NiO_x/W:$BiVO_4$	0.8 V_{RHE}	GALD, GCALD, DHA, FA, FMALD	R_{DHA}, R_{GCALD}, R_{FA} FE_{DHA}, FE_{FA}
		1.2 V_{RHE}	GALD, GCALD, DHA, FA, FMALD	

Product analysis and identification enabled us to propose reaction path(s) for the photoelectrocatalytic glycerol decomposition using W:$BiVO_4$ and NiO_x/W:$BiVO_4$ electrodes. It is proposed that DHA and GALD isomers are the first stable species to form upon $2e^-$ oxidation of one of the hydroxyl moieties of glycerol.[33-34] A higher yield of DHA compared to GALD (Fig. 3) corroborates with DFT calculations that have identified DHA as the thermodynamically more stable product than GALD.[35] GCALD is proposed to form from isomeric DHA/GALD species through C–C bond cleavage, releasing one equivalent of FA. Subsequent C–C bond cleavage to form one more equivalent of FA and FMALD from GCALD is proposed as one of the further steps.

3.2. Fundamental activity design principles for oxygen evolution catalysts

RuO_x and IrO_x currently serve as benchmark OER electrocatalysts because of their high activity and stability, particularly in acidic conditions, featuring performances unmatched by catalysts based on non-precious metals.[6] However, the scarcity and high costs of noble metals limit widespread exploitation of RuO_x and IrO_x. Pyrochlore materials with the general formula $A_2B_2O_{7-\delta}$ (A is typically a rare-earth or alkaline-earth metal, B is a transition metal) have emerged recently as promising alternatives to binary RuO_x and IrO_x oxides owing to their lower noble metal content and high activity in OER.[36] Metal substitution is a common strategy to tune the activity of complex oxides since a substituent can induce changes in the oxidation state of the active metal, the concentration of oxygen vacancies (V_O), the coordination environments, the electronic band structure, *etc*. Since multiple structural properties are simultaneously affected by substitution, it becomes challenging to identify the contribution of each individual variable on the kinetics of the catalytic reaction. Therefore, it is of fundamental importance to reveal the physical origin of the substitution effect in complex oxides on the OER activity, as such an understanding can guide the rational design of the new compositions for OER.

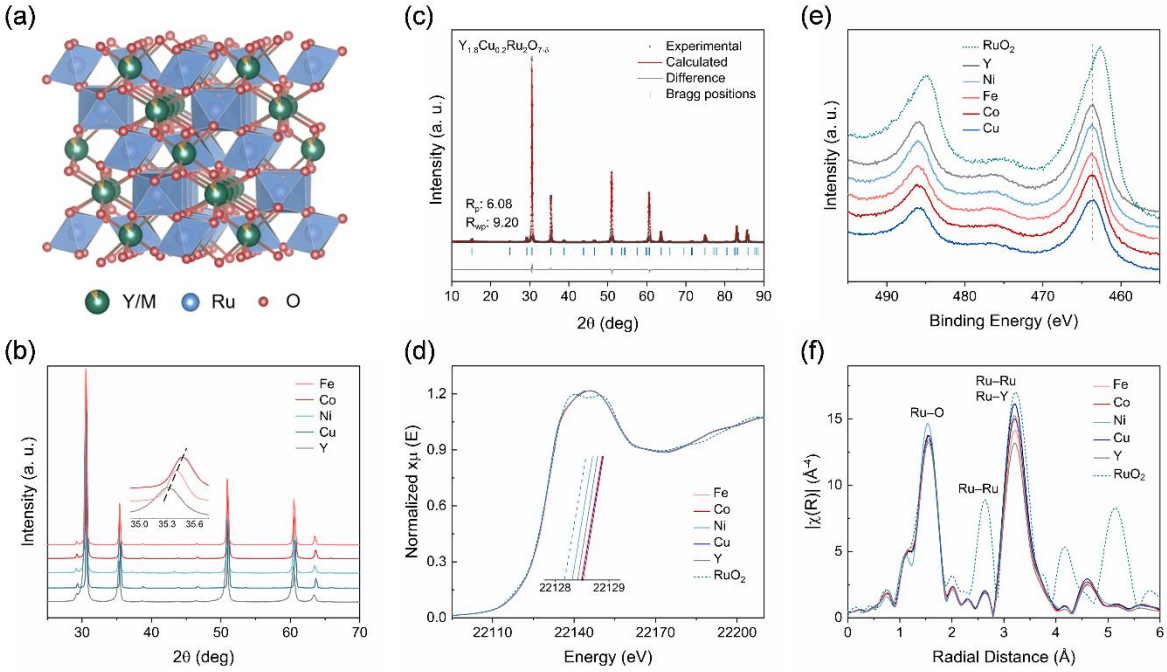

Figure 4. (a) Crystal structure of $Y_{1.8}M_{0.2}Ru_2O_{7-\delta}$ with the A-sites occupied by Y^{3+} and M^{n+} ions. (b) XRD patterns of $Y_{1.8}M_{0.2}Ru_2O_{7-\delta}$. Inset: shifts of the (400) peak upon substitution of Y^{3+} by smaller M^{n+} ions. (c) Rietveld refinement for $Y_{1.8}Cu_{0.2}Ru_2O_{7-\delta}$. Comparison of RuO_2 and $Y_{1.8}M_{0.2}Ru_2O_{7-\delta}$ pyrochlores including (d) normalized Ru K-edge XANES, (e) Ru 3d core level XPS, and (f) phase-uncorrected Fourier-transform of the Ru K-edge EXAFS functions. For brevity, M represents $Y_{1.8}M_{0.2}Ru_2O_{7-\delta}$ on the legends.

To disclose the role of metal substitution on the catalyst's activity, we have prepared $Y_{1.8}M_{0.2}Ru_2O_{7-\delta}$ pyrochlores (M = Fe, Co, Ni, Cu, Y, Fig. 4a) motivated by the excellent structural and surface stability of $Y_2Ru_2O_{7-\delta}$ under OER conditions, where a moderate level of A-site substitution was employed to keep the ruthenium oxidation state unchanged within the series. Powder X-ray diffraction (XRD) data (Fig. 4b, c) confirm the successful incorporation of the M substituent in the pyrochlore structure, shown by a decrease of the unit cell parameters for all substituents according to Rietveld refinement. Energy-dispersive X-ray (EDX) spectroscopy reveals a homogeneous distribution of metals in the materials. XRD data indicate that pyrochlores were obtained phase pure. Only a minor difference in the position of the Ru K-edge is observed in X-ray absorption near edge structure (XANES) spectra of $Y_{1.8}M_{0.2}Ru_2O_{7-\delta}$ (Fig. 4d). This provides a strong indication that the oxidation state of Ru is unaffected by substitution for the entire $Y_{1.8}M_{0.2}Ru_2O_{7-\delta}$ series. Ru 3d core level X-ray photoelectron spectra (XPS) are in agreement with XANES data as the position of the Ru $3d_{5/2}$ peak is constant at ~ 464 eV in the $Y_{1.8}M_{0.2}Ru_2O_{7-\delta}$ materials, confirming the same oxidation state of Ru that is slightly higher than in RuO_2 (Fig. 4e). The local coordination environment of the Ru atoms in $Y_{1.8}M_{0.2}Ru_2O_{7-\delta}$ was inferred from the Fourier transform extended X-ray absorption fine structure (EXAFS) spectra. The extracted fitting parameters of the experimental Ru K-edge EXAFS data agree with the crystallographic model (Fig. 4a). The first coordination sphere of Ru was fitted by a Ru−O scattering path at ~1.99 Å and the second shell was modelled by Ru−Ru and Ru−Y contacts at ~ 3.58 Å (Fig. 4f).

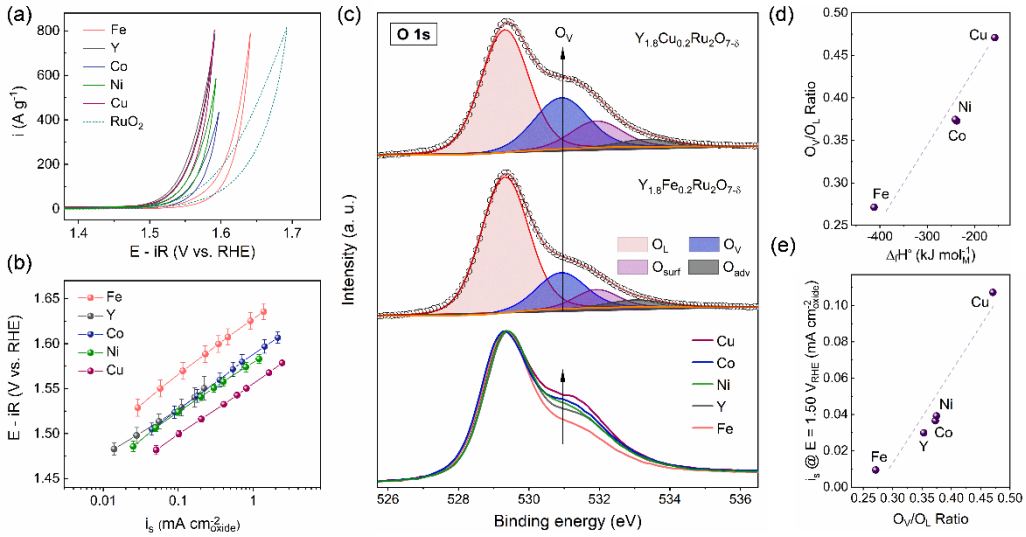

Figure 5. (a) Representative CV curves for $Y_{1.8}M_{0.2}Ru_2O_{7-\delta}$ pyrochlores (for brevity, only the M substituent is shown in the legends) and the RuO_2 benchmark recorded in 1 N H_2SO_4. (b) Tafel plots derived from steady-state galvanostatic measurements with currents normalized by BET surface area of the oxides. (c) Overlay of the O 1s core level XPS spectra for $Y_{1.8}M_{0.2}Ru_2O_{7-\delta}$ highlighting the emergence of a feature at ~ 531 eV along with the fitted spectra for $Y_{1.8}M_{0.2}Ru_2O_{7-\delta}$ (M = Cu, Fe) oxides. All spectra were normalized by the same maximum of the intensity. (d) Relation between the O_V/O_L ratio and enthalpies of MO_x formation, Δ_fH^o, given per mol of metal. (e) Scaling between OER activity of $Y_{1.8}M_{0.2}Ru_2O_{7-\delta}$, defined as current density measured at potential 1.50 V vs. RHE and oxygen vacancies content expressed as O_V/O_L ratio. Dotted lines are to guide the eye.

Next, we assessed an OER activity for the $Y_{1.8}M_{0.2}Ru_2O_{7-\delta}$ series in 1 N H_2SO_4. All prepared $Y_{1.8}M_{0.2}Ru_2O_{7-\delta}$ pyrochlores feature similar Tafel slopes in the range of 52–63 mV dec^{-1} indicative of the same rate-limiting step. Notably, while the substitution of Y by Fe is detrimental for the OER activity, the incorporation of Cu increases the OER activity of $Y_{1.8}Cu_{0.2}Ru_2O_{7-\delta}$ vs. $Y_{1.8}Fe_{0.2}Ru_2O_{7-\delta}$ by more than one order of magnitude (estimated by the specific current density at 1.50 V vs. RHE, Fig. 5b). The superior OER activity of $Y_{1.8}Cu_{0.2}Ru_2O_{7-\delta}$ with respect to unsubstituted $Y_2Ru_2O_{7-\delta}$ is remarkable considering that $Y_{2+x}Ru_{2-x}O_{7-\delta}$ (x = 0, 0.4) oxides have been introduced only recently as OER catalysts with benchmark performances in acidic media. Remarkably, $Y_{1.8}Cu_{0.2}Ru_2O_{7-\delta}$ also features excellent stability under galvanostatic OER conditions.

The density of the oxygen vacancy (V_O) sites at the surface in $Y_{1.8}M_{0.2}Ru_2O_{7-\delta}$ was studied to establish its potential correlations with the OER activity. The oxygen states at the surface in $Y_{1.8}M_{0.2}Ru_2O_{7-\delta}$ were probed by O 1s core level XPS. Clearly, the ratio O_V/O_L (O_V stands for oxygen atoms in the vicinity of O vacancies in the lattice, O_L – oxygen lattice atoms) scales with the density of surface oxygen vacancies in the pyrochlore and it is also indicative of the varied lability of the lattice oxygen in $Y_{1.8}M_{0.2}Ru_2O_{7-\delta}$. We find that a greater OER activity correlates with a higher concentration of V_O sites and ultimately with the enthalpy of formation of the binary oxides MO_x (Fig. 5d, e).

Density functional theory (DFT) calculations were employed to rationalize the differences in the energies of V_O formation and the OER activities for $Y_{1.8}M_{0.2}Ru_2O_{7-\delta}$ pyrochlores. We have found, that the intrinsic OER activity of the $Y_{1.8}M_{0.2}Ru_2O_7$ family correlates linearly with the position of the O *2p* band center computed for surface O atoms (Fig. 6c). Therefore, a decreased energy gap between the O *2p* states and the Fermi level (or separation between the O *2p* and Ru *4d* band centers, defining the charge transfer energy) governs the experimental OER activity of the Ru pyrochlores studied here.

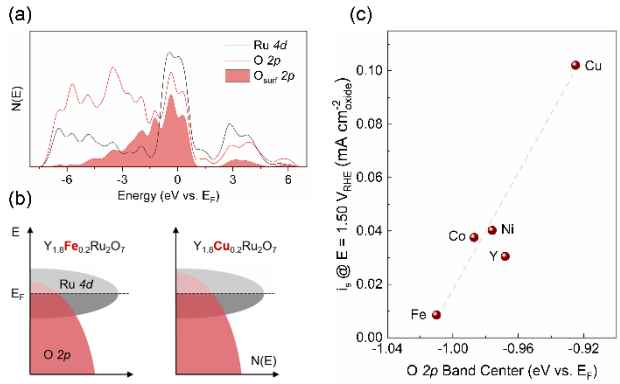

Figure 6. (a) Projected density of states (DOS) on Ru *4d* and O *2p* states of $Y_{1.8}Cu_{0.2}Ru_2O_7$. Projected DOS on O *2p* states of surface terminated oxygen atoms (O_{surf}) are shaded. (b) Schematic rigid band diagram for $Y_{1.8}Fe_{0.2}Ru_2O_7$ and $Y_{1.8}Cu_{0.2}Ru_2O_7$ illustrating an upshift of the O *2p* band center, facilitating the loss of lattice oxygen, creation of V_O sites and enhancement of OER activity. (c) Correlation between $Y_{1.8}M_{0.2}Ru_2O_{7-\delta}$ specific OER activity estimated as current density at 1.50 V vs. RHE and O *2p* band center position. Error bars for i_s are smaller than the data points. Dotted line is to guide the eye.

Having established the link between the lability of surface oxygen and the OER activity in $Y_{1.8}M_{0.2}Ru_2O_7$ electrocatalysts, we searched to relate further these experimental observations to physical properties of binary oxides MO_x. We reasoned that if such correlation is found, it will enable a rational design of active OER catalysts. Indeed, the density of V_O sites and OER activities of $Y_{1.8}M_{0.2}Ru_2O_7$ catalysts scales with the enthalpies of formation ($\Delta_fH°$) of the binary oxides MO_x (Fe_2O_3, CoO, NiO, CuO). A less negative $\Delta_fH°$ of MO_x (*i.e.* less stable oxide) correlates with an increased density of V_O sites in $Y_{1.8}M_{0.2}Ru_2O_{7-\delta}$ (Fig. 5d) as weaker M–O bonds facilitate the removal of lattice oxygen atoms, enhancing the OER kinetics.

3.3. Design of the non-precious metal-based catalysts for hydrogen evolution reaction

Oxidation of glycerol (or any other substrate) on a (photo)anode in a (photo)electrochemical cell is accompanied by a reduction reaction at the cathode. In aqueous solutions, hydrogen evolution via proton reduction typically occurs on the cathodic side. Metallic platinum is currently the benchmark catalyst for the hydrogen evolution reaction, however its low abundance and high cost motivates for the search of non-noble metal-based materials that are active in HER.

Two dimensional early transition metal (TM) carbides, nitrides and carbonitrides, known as MXenes, form a family of materials exploited in many areas including energy research.[37] Several members of the MXene family, for instance Mo_2CT_x, have been introduced recently as promising catalysts for the hydrogen evolution reaction (HER) in acidic conditions.[20] The high activity of Mo_2CT_x was attributed to favorable thermodynamics of the hydrogen binding on the Mo_2CT_x (T_x = O/OH) surface, with a close-to-zero free energy of hydrogen adsorption (ΔG_H). The latter parameter is considered as the primary descriptor for the HER activity across a variety of material classes.[38] A series of theoretical studies on 2D carbide/nitride structures established that the H adsorption energy can be tuned effectively by a sub-monolayer coverage of the surface with transition metal ad-atoms, rendering TM-promoted materials efficient HER catalysts.[39-40] These predictions, however, so far lack experimental validation due to the absence of synthetic approaches for such TM-modified 2D catalysts. The incorporation of a metal dopant into a MXene matrix not only introduces an additional reaction site, but can also alter the adsorption energetics of the surface, for instance the binding energies for electrocatalytic intermediates (e.g. adsorbed *H, *OH, *O), thereby influencing the reaction kinetics.

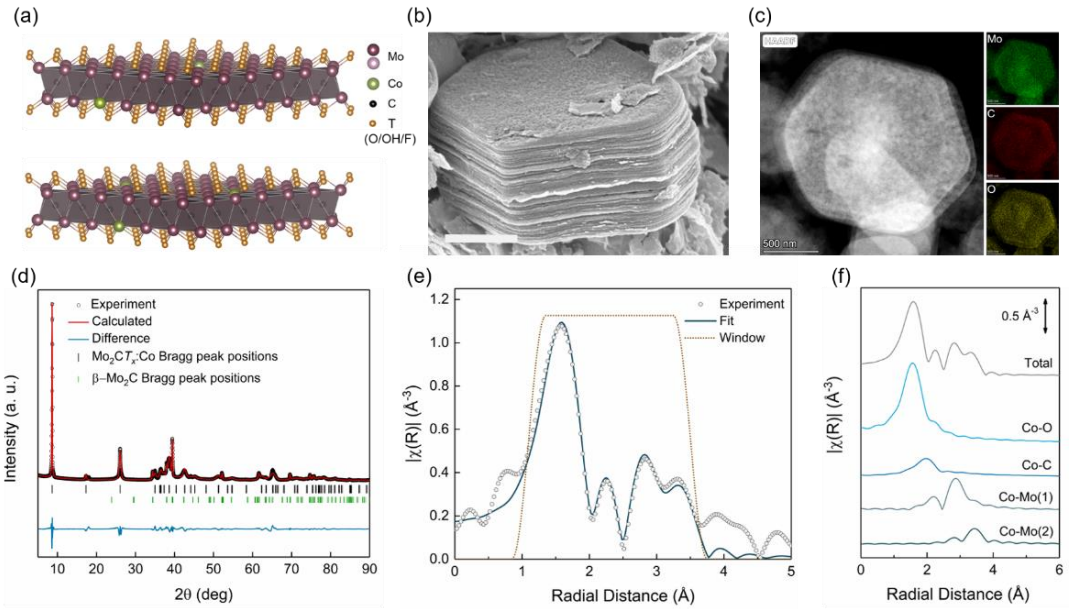

Figure 7. (a) Schematic representation of the Mo_2CT_x:Co structure used for fitting of the EXAFS data acquired. The model substitutes a Mo atom by Co in the parent Mo_2CT_x assuming that the surface is fully terminated by oxygen groups. (b) SEM image of Mo_2CT_x:Co showing stacked layers with platelet morphology; the scale bar is 500 nm. (c) HAADF-STEM image and elemental mapping for delaminated Mo_2CT_x:Co sheets demonstrating a uniform distribution of Mo, C and O atoms within the sheets. The concentration of Co substitution is too low to be reliably detected by EDX mapping. (d) Le Bail fit for Mo_2CT_x:Co material revealing that all reflections could be assigned to Mo_2CT_x and β-Mo_2C phases. (e) Phase-uncorrected Fourier-transform of the Co K-edge EXAFS function for Mo_2CT_x:Co and its fit using the model shown in panel (a). (f) Single scattering paths used in the EXAFS fit.

To this end, we have designed and performed the synthesis and detailed characterization of a cobalt substituted MXene material, Mo_2CT_x:Co. The developed methodology uses a bulk β-Mo_2C phase for the incorporation of cobalt atoms (β-Mo_2C:Co) that are retained in the final Mo_2CT_x:Co structure during the synthesis (Scheme 2). The synthesis yields layered platelets of the two-dimensional Mo_2CT_x:Co MXene phase, as confirmed by scanning and transmission electron microscopies (SEM/TEM, Fig. 7a, b).

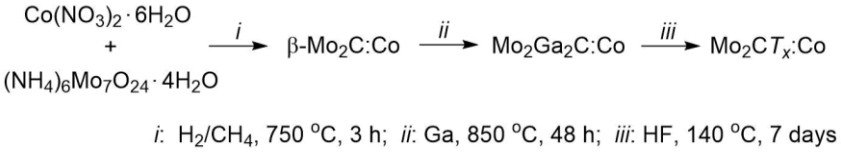

Scheme 2. Synthesis of Mo_2CT_x:Co.

EXAFS analysis (Fig. 7e, f) of the synthesized MXene material unequivocally confirms that isolated cobalt atoms are incorporated into the Mo_2CT_x lattice, adopting the same coordination geometry as the host molybdenum sites, consistent with the formation of a solid solution, while XRD data reveal the absence of any other Co-containing phases (Fig. 7d).

To assess the effect of cobalt substitution on the electronic structure and catalytic properties of Mo_2CT_x:Co, we have probed its activity for the hydrogen evolution reaction (HER) in acidic conditions since the parent Mo_2CT_x material already demonstrated a promising performance for this reaction. Noteworthy, we observed a substantial increase of the catalytic performance of Mo_2CT_x:Co relative to the unsubstituted Mo_2CT_x material. Our density functional theory (DFT) calculations show that even a small amount of Co in the Mo_2CT_x lattice imparts a significant perturbation in the electronic structure of Mo_2CT_x:Co. In particular, the substitution of Mo by Co affects the adsorption energies of hydrogen on

the neighboring oxygen atoms of an oxygen-terminated Mo_2CO_2:Co surface, making these sites more favorable for HER catalysis.

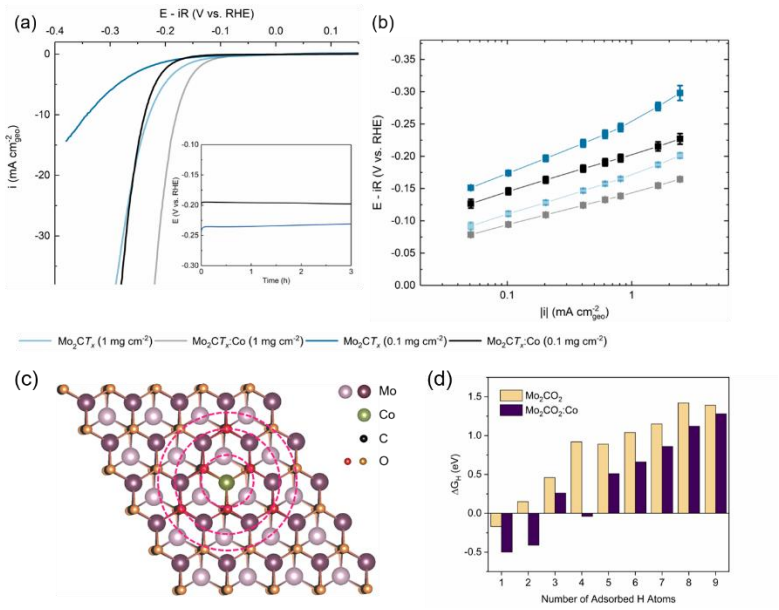

Figure 8. (a) Polarization curves recorded for Mo_2CT_x:Co and Mo_2CT_x using a scan rate of 10 mV s^{-1}. Inset shows chronopotentiometry data for both catalysts at 0.1 mg cm^{-2} loading held at 1 mA cm_{geo}^{-2}. Tafel plots derived from steady-state galvanostatic measurements with currents normalized per geometric electrode area. Error bars represent standard deviation obtained from at least 3 independent measurements. (c) Mo_2CO_2 :Co model structure used for DFT calculations. Dashed circles are drawn to define areas containing O atoms, which were used as hydrogen adsorption sites in computations. The six nearest oxygen atoms featuring the highest deviation in ΔG_H for the substituted and non-substituted cases are shown in red. (d) Computed values of the free energies of hydrogen adsorption (ΔG_H) on Mo_2CO_2 and Mo_2CO_2:Co surfaces.

Notably, Mo_2CT_x:Co features an excellent durability under acidic HER conditions maintaining a constant potential to achieve a current density of 1 mA cm^{-2} over 3 hours (Figure 8a, inset). Supplemented by a very low onset potential for HER (above −70 mV vs RHE), all of the activity metrics highlight that Mo_2CT_x:Co is one of the best performing HER catalysts reported so far. Importantly, these results validate the metal-substitution approach of Mo_2CT_x as a valuable tool to provide compositionally-tunable materials for electrocatalysis and introduce Mo_2CT_x:Co as a novel benchmark catalyst for HER.

4 Conclusions

1. Our study revealed the key trends in the product distribution of the photoelectrochemical glycerol oxidation over $BiVO_4$-based electrodes in the presence/absence of a NiO_x co-catalyst, at varying electrolyte environments. We have found that GALD, DHA, GCALD, FA and FMALD are the primary products of glycerol oxidation. To the best of our knowledge, in this study GCALD was detected as a product of PEC glycerol oxidation for the first time. Importantly, we identify the conditions favouring the formation of the high value-added chemicals, DHA and GALD, thus providing a rare example of a system enabling the production of valuable C_3 products from glycerol without the use of precious metal catalysts. The reported development of a system for the photoelectrochemical glycerol reforming relying on earth-

abundant elements is an important step in the advancement of affordable solar-driven electrolyzers and direct alcohol fuel cells.

2. Using $Y_{1.8}M_{0.2}Ru_2O_{7-\delta}$ as a model system, we have identified a direct correlation between the OER activity, the lattice oxygen binding strength/lability and the formation enthalpy of the binary MO_x oxide, *i.e.* metals M with lower enthalpies of formation for the respective oxide weaken the oxygen binding on the surface of $Y_{1.8}M_{0.2}Ru_2O_{7-\delta}$. DFT studies captured changes in the electronic structure of the pyrochlores induced by M substitution and revealed trends in the electronic band structure that govern the OER activity of the $Y_{1.8}M_{0.2}Ru_2O_{7-\delta}$ catalysts. Specifically, an increase in the density of V_O sites and the OER activity in $Y_{1.8}M_{0.2}Ru_2O_{7-\delta}$ is attributed to the upshift of the O *2p* band centre closer to the Fermi level. Our work introduces $Y_{1.8}Cu_{0.2}Ru_2O_{7-\delta}$ as a novel OER catalyst with exceptional OER performance and, more fundamentally, emphasizes the underexplored role that substituents can play in regulating the OER activity of complex oxides, *i.e.* by influencing the surface oxygen binding strength. Our results can be utilized for the rational design of new compositions for oxygen electrocatalysis and other applications that involve lattice oxygen sites.

3. We reported the synthesis and the comprehensive characterization of a solid solution Mo_2CT_x:Co MXene phase with cobalt substitution on the molybdenum sites as an very active catalyst for the hydrogen evolution reaction. Mo_2CT_x:Co displays an impressive performance in HER concerning both its durability and activity, with the latter being notably higher than that of unsubstituted Mo_2CT_x. DFT calculations attribute the enhancement of the HER activity upon cobalt substitution to improved thermodynamics of the hydrogen binding on the MXene surface thereby facilitating the H_2 evolution reaction. Importantly, our synthetic strategy represents a new approach for the preparation of 2D molybdenum carbides containing single metal site substitution and it opens up the prospects of accessing materials incorporating other TMs, where the substituent can be tailored for a specific catalytic application.

5 Outlook and next steps

Considering the current state of the progress along three research directions outlined in section 3, we consider the continuation of the project towards realization of the following fundamental and practical tasks particularly promising.

1. Through the investigation of the model systems ($A_2Ir_2O_{7-\delta}$/$A_xFe_{3-x}O_4$), our study aims to provide a general fundamental insight on the effect of elemental substitution in complex oxides on their electronic structure, redox and catalytic properties. A focus of our study is a survey for new compositions for oxygen electrocatalysis (OER/ORR) with improved performance, based on the insights gained from the model study, aided by DFT. By completing the proposed goals, we expect to build a robust and comprehensive scheme rationalizing the influence of cation substitution on the OER/ORR performance of complex oxides and provide a novel guideline for the design of materials for oxygen electrocatalysis that is cornerstone for renewable energy technologies.

2. Fundamental understanding of the effect of alloying on the electronic structure, redox and catalytic properties (primarily for the methanol oxidation reaction) of the noble metal-based alloys and intermetallic compounds. Given the high activity and widespread use of noble metals in numerous lab-scale and industrially relevant processes, we anticipate that fundamental insights provided by our study can have an impact in multiple areas. Our particular focus is on the development of efficient catalysts for methanol electrooxidation and their implementation as anode materials in the direct methanol fuel cells. Finding the stoichiometry featuring a reduced noble metal content without compromising performance would certainly become a crucial step towards the promotion of this type of devices, which are expected to be a key element in a sustainable energy world.

6 National and international cooperation

Dr. P.V. Kumar (UNSW, Australia) – DFT calculations;

Dr. O.V. Safonova (PSI, Switzerland) – synchrotron XAS measurements;

Dr. N.C. Pflug, Prof. K. McNeill (ETH Zürich, Switzerland) – NMR measurements.

7 Publications within the project

(1) Kuznetsov, D. A.; Chen, Z.; Kumar, P. V.; Tsoukalou, A.; Kierzkowska, A.; Abdala, P. M.; Safonova, O. V.; Fedorov, A.; Müller, C. R. Single Site Cobalt Substitution in 2D Molybdenum Carbide (MXene) Enhances Catalytic Activity in the Hydrogen Evolution Reaction. *J. Am. Chem. Soc.*, 2019, 141, 17809-17816 (selected as the journal cover page).

(2) Kuznetsov, D. A.; Naeem, M. A.; Kumar, P. V.; Abdala, P. M.; Fedorov, A.; Müller, C. R. Tailoring Lattice Oxygen Binding in Ruthenium Pyrochlores to Enhance Oxygen Evolution Activity. *J. Am. Chem. Soc.*, 2020, 142, 7883-7888 (selected as the journal cover page).

(3) Wu, Y.-H.; Kuznetsov, D. A.; Pflug, N. C.; Fedorov, A.; Müller, C. R. Solar-driven valorisation of glycerol on $BiVO_4$ photoanodes: effect of co-catalyst and reaction media on reaction selectivity. *Submitted*.

8 References

(1) Stamenkovic, V. R.; Strmcnik, D.; Lopes, P. P.; Markovic, N. M., Energy and Fuels from Electrochemical Interfaces. *Nat. Mater.* **2016,** *16*, 57-69.

(2) Staffell, I.; Scamman, D.; Velazquez Abad, A.; Balcombe, P.; Dodds, P. E.; Ekins, P.; Shah, N.; Ward, K. R., The role of hydrogen and fuel cells in the global energy system. *Energy Environ. Sci.* **2019,** *12*, 463-491.

(3) Foster, S. L.; Bakovic, S. I. P.; Duda, R. D.; Maheshwari, S.; Milton, R. D.; Minteer, S. D.; Janik, M. J.; Renner, J. N.; Greenlee, L. F., Catalysts for Nitrogen Reduction to Ammonia. *Nat. Catal.* **2018,** *1*, 490-500.

(4) Porosoff, M. D.; Yan, B.; Chen, J. G., Catalytic reduction of CO2 by H2 for synthesis of CO, methanol and hydrocarbons: challenges and opportunities. *Energy Environ. Sci.* **2016,** *9*, 62-73.

(5) Davis, S. J.; Lewis, N. S.; Shaner, M.; Aggarwal, S.; Arent, D.; Azevedo, I. L.; Benson, S. M.; Bradley, T.; Brouwer, J.; Chiang, Y.-M.; Clack, C. T. M.; Cohen, A.; Doig, S.; Edmonds, J.; Fennell, P.; Field, C. B.; Hannegan, B.; Hodge, B.-M.; Hoffert, M. I.; Ingersoll, E.; Jaramillo, P.; Lackner, K. S.; Mach, K. J.; Mastrandrea, M.; Ogden, J.; Peterson, P. F.; Sanchez, D. L.; Sperling, D.; Stagner, J.; Trancik, J. E.; Yang, C.-J.; Caldeira, K., Net-zero emissions energy systems. *Science* **2018,** *360*, eaas9793.

(6) McCrory, C. C. L.; Jung, S.; Ferrer, I. M.; Chatman, S. M.; Peters, J. C.; Jaramillo, T. F., Benchmarking Hydrogen Evolving Reaction and Oxygen Evolving Reaction Electrocatalysts for Solar Water Splitting Devices. *J. Am. Chem. Soc.* **2015,** *137*, 4347-4357.

(7) Montoya, J. H.; Seitz, L. C.; Chakthranont, P.; Vojvodic, A.; Jaramillo, T. F.; Norskov, J. K., Materials for Solar Fuels and Chemicals. *Nat. Mater.* **2017,** *16*, 70-81.

(8) Walter, M. G.; Warren, E. L.; McKone, J. R.; Boettcher, S. W.; Mi, Q.; Santori, E. A.; Lewis, N. S., Solar Water Splitting Cells. *Chem. Rev.* **2010,** *110*, 6446-6473.

(9) Wakerley, D. W.; Kuehnel, M. F.; Orchard, K. L.; Ly, K. H.; Rosser, T. E.; Reisner, E., Solar-driven reforming of lignocellulose to H2 with a CdS/CdOx photocatalyst. *Nat. Energy* **2017,** *2*, 17021.
(10) Mondelli, C.; Gözaydın, G.; Yan, N.; Pérez-Ramírez, J., Biomass valorisation over metal-based solid catalysts from nanoparticles to single atoms. *Chem. Soc. Rev.* **2020,** *49*, 3764-3782.
(11) Sivula, K.; van de Krol, R., Semiconducting materials for photoelectrochemical energy conversion. *Nat. Rev. Mater.* **2016,** *1*, 15010.
(12) Meher, L. C.; Sagar, D. V.; Naik, S. N., Technical aspects of biodiesel production by transesterification—a review. *Renew. Sustain. Energy Rev.* **2006,** *10*, 248-268.
(13) Simões, M.; Baranton, S.; Coutanceau, C. J. C., Electrochemical valorisation of glycerol. *ChemSusChem* **2012,** *5*, 2106-2124.
(14) Zakaria, K.; McKay, M.; Thimmappa, R.; Hasan, M.; Mamlouk, M.; Scott, K., Direct Glycerol Fuel Cells: Comparison with Direct Methanol and Ethanol Fuel Cells. *ChemElectroChem* **2019,** *6*, 2578-2585.
(15) Zhang, Z.; Xin, L.; Qi, J.; Chadderdon, D. J.; Li, W., Supported Pt, Pd and Au nanoparticle anode catalysts for anion-exchange membrane fuel cells with glycerol and crude glycerol fuels. *Appl. Catal. B-Environ.* **2013,** *136-137*, 29-39.
(16) Kudo, A.; Omori, K.; Kato, H., A novel aqueous process for preparation of crystal form-controlled and highly crystalline BiVO4 powder from layered vanadates at room temperature and its photocatalytic and photophysical properties. *J. Am. Chem. Soc.* **1999,** *121*, 11459-11467.
(17) Kudo, A.; Ueda, K.; Kato, H.; Mikami, I., Photocatalytic O2 evolution under visible light irradiation on BiVO4 in aqueous AgNO3 solution. *Catal. Lett.* **1998,** *53*, 229-230.
(18) Tokunaga, S.; Kato, H.; Kudo, A., Selective Preparation of Monoclinic and Tetragonal BiVO4 with Scheelite Structure and Their Photocatalytic Properties. *Chem. Mater.* **2001,** *13*, 4624-4628.
(19) Moniz, S. J. A.; Shevlin, S. A.; Martin, D. J.; Guo, Z.-X.; Tang, J., Visible-light driven heterojunction photocatalysts for water splitting – a critical review. *Energy Environ. Sci.* **2015,** *8*, 731-759.
(20) Seh, Z. W.; Fredrickson, K. D.; Anasori, B.; Kibsgaard, J.; Strickler, A. L.; Lukatskaya, M. R.; Gogotsi, Y.; Jaramillo, T. F.; Vojvodic, A., Two-Dimensional Molybdenum Carbide (MXene) as an Efficient Electrocatalyst for Hydrogen Evolution. *ACS Energy Lett.* **2016,** *1*, 589-594.
(21) Dincă, M.; Surendranath, Y.; Nocera, D. G., Nickel-Borate Oxygen-Evolving Catalyst that Functions under Benign Conditions. *Proc. Natl. Acad. Sci U. S. A.* **2010,** *107*, 10337.
(22) McDonald, K. J.; Choi, K.-S., A new electrochemical synthesis route for a BiOI electrode and its conversion to a highly efficient porous BiVO4 photoanode for solar water oxidation. *Energy Environ. Sci.* **2012,** *5*, 8553-8557.
(23) Lee, D. K.; Choi, K.-S., Enhancing long-term photostability of BiVO4 photoanodes for solar water splitting by tuning electrolyte composition. *Nat. Energy* **2018,** *3*, 53-60.
(24) Park, H. S.; Kweon, K. E.; Ye, H.; Paek, E.; Hwang, G. S.; Bard, A. J., Factors in the Metal Doping of BiVO4for Improved Photoelectrocatalytic Activity as Studied by Scanning Electrochemical Microscopy and First-Principles Density-Functional Calculation. *J. Phys. Chem. C* **2011,** *115*, 17870-17879.
(25) Asundi, A. S.; Raiford, J. A.; Bent, S. F., Opportunities for Atomic Layer Deposition in Emerging Energy Technologies. *ACS Energy Lett.* **2019,** *4*, 908-925.
(26) Ratcliff, E. L.; Meyer, J.; Steirer, K. X.; Garcia, A.; Berry, J. J.; Ginley, D. S.; Olson, D. C.; Kahn, A.; Armstrong, N. R., Evidence for near-surface NiOOH species in solution-processed NiO x selective interlayer materials: impact on energetics and the performance of polymer bulk heterojunction photovoltaics. *Chem. Mater.* **2011,** *23*, 4988-5000.
(27) Stoerzinger, K. A.; Hong, W. T.; Wang, X. R.; Rao, R. R.; Subramanyam, S. B.; Li, C. J.; Ariando; Venkatesan, T.; Liu, Q.; Crumlin, E. J.; Varanasi, K. K.; Shao-Horn, Y., Decreasing the Hydroxylation Affinity of $La_{1-x}Sr_xMnO_3$ Perovskites To Promote Oxygen Reduction Electrocatalysis. *Chem. Mater.* **2017,** *29*, 9990-9997.

(28) Trotochaud, L.; Ranney, J. K.; Williams, K. N.; Boettcher, S. W., Solution-cast metal oxide thin film electrocatalysts for oxygen evolution. *J. Am. Chem. Soc.* **2012,** *134*, 17253-17261.
(29) Lu, X.; Xie, S.; Yang, H.; Tong, Y.; Ji, H., Photoelectrochemical hydrogen production from biomass derivatives and water. *Chem. Soc. Rev.* **2014,** *43*, 7581-93.
(30) Görlin, M.; Ferreira de Araújo, J.; Schmies, H.; Bernsmeier, D.; Dresp, S.; Gliech, M.; Jusys, Z.; Chernev, P.; Kraehnert, R.; Dau, H.; Strasser, P., Tracking Catalyst Redox States and Reaction Dynamics in Ni–Fe Oxyhydroxide Oxygen Evolution Reaction Electrocatalysts: The Role of Catalyst Support and Electrolyte pH. *J. Am. Chem. Soc.* **2017,** *139*, 2070-2082.
(31) Hagfeldt, A.; Lindström, H.; Södergren, S.; Lindquist, S.-E., Photoelectrochemical studies of colloidal TiO2 films: the effect of oxygen studied by photocurrent transients. *J. Electroanal. Chem.* **1995,** *381*, 39-46.
(32) Liu, D.; Liu, J. C.; Cai, W.; Ma, J.; Yang, H. B.; Xiao, H.; Li, J.; Xiong, Y.; Huang, Y.; Liu, B., Selective photoelectrochemical oxidation of glycerol to high value-added dihydroxyacetone. *Nat. Commun.* **2019,** *10*, 1779.
(33) Dai, C.; Sun, L.; Liao, H.; Khezri, B.; Webster, R. D.; Fisher, A. C.; Xu, Z. J., Electrochemical production of lactic acid from glycerol oxidation catalyzed by AuPt nanoparticles. *J. Catal.* **2017,** *356*, 14-21.
(34) Simões, M.; Baranton, S.; Coutanceau, C., Electro-oxidation of glycerol at Pd based nano-catalysts for an application in alkaline fuel cells for chemicals and energy cogeneration. *Appl. Catal. B-Environ.* **2010,** *93*, 354-362.
(35) Cheng, L.; Doubleday, C.; Breslow, R., Evidence for tunneling in base-catalyzed isomerization of glyceraldehyde to dihydroxyacetone by hydride shift under formose conditions. *Proc. Natl. Acad. Sci. U. S. A.* **2015,** *112*, 4218-20.
(36) Kim, J.; Shih, P.-C.; Tsao, K.-C.; Pan, Y.-T.; Yin, X.; Sun, C.-J.; Yang, H., High-Performance Pyrochlore-Type Yttrium Ruthenate Electrocatalyst for Oxygen Evolution Reaction in Acidic Media. *J. Am. Chem. Soc.* **2017,** *139*, 12076-12083.
(37) Anasori, B.; Lukatskaya, M. R.; Gogotsi, Y., 2D metal carbides and nitrides (MXenes) for energy storage. *Nat. Rev. Mater.* **2017,** *2*, 16098.
(38) Nørskov, J. K.; Bligaard, T.; Logadottir, A.; Kitchin, J. R.; Chen, J. G.; Pandelov, S.; Stimming, U., Trends in the Exchange Current for Hydrogen Evolution. *J. Electrochem. Soc.* **2005,** *152*, J23-J26.
(39) Ling, C.; Shi, L.; Ouyang, Y.; Chen, Q.; Wang, J., Transition Metal-Promoted V2CO2 (MXenes): A New and Highly Active Catalyst for Hydrogen Evolution Reaction. *Adv. Sci.* **2016,** *3*, 1600180.
(40) Li, P.; Zhu, J.; Handoko, A. D.; Zhang, R.; Wang, H.; Legut, D.; Wen, X.; Fu, Z.; Seh, Z. W.; Zhang, Q., High-throughput theoretical optimization of the hydrogen evolution reaction on MXenes by transition metal modification. *J. Mater. Chem. A* **2018,** *6*, 4271-4278.